FULL PAPER

Energy Storage

ADVANCED
FUNCTIONAL
MATERIALS

www.afm-journal.de

Bioinspired Micro/Nanofluidic Ion Transport Channels for Organic Cathodes in High-Rate and Ultrastable Lithium/Sodium-Ion Batteries

Gangyong Zhou, Yue-E Miao,* Zengxi Wei, LuLu Mo, Feili Lai, Yue Wu, Jianmin Ma,* and Tianxi Liu*

Conjugated carbonyl compounds are considered as ideal substitutes for traditional inorganic electrodes in lithium/sodium ion batteries (LIBs/SIBs) due to their excellent redox reversibility and structural tunability. Here, a flexible sandwich-structured 3,4,9,10-perylenetetracarboxylic dianhydride (PTCDA)/reduced graphene oxide (RGO)/carbon nanotube (CNT) (PTCDA/RGO/CNT) composite film with bioinspired micro/nanofluidic ion transport channels and interconnected porous conductive frameworks is designed and obtained by vacuum-filtration and heating methods for LIB/SIB applications. The PTCDA/RGO/CNT electrode with robust mechanical deformability exhibits high diffusion coefficients of Li$^+$/Na$^+$ and low Warburg coefficients. Thus, desirable electrochemical performances with high capacities of 131 and 126 mA h g^{-1} at 10 mA g^{-1}, and ultralong cycling stability with over 99% capacity retention after 500 cycles at 200 mA g^{-1} are achieved for LIBs and SIBs, respectively. In particular, Li/Na-ion full cells consisting of lithiated or sodiated electrospun carbon nanofiber anode and PTCDA/RGO/CNT-based cathode are developed to exhibit high energy densities of 132.6 and 104.4 W h kg^{-1} at the power densities of 340 and 288 W kg^{-1} for LIBs and SIBs, respectively. The advantageous features demonstrated by constructing bioinspired micro/nanofluidic channels may provide a new pathway toward the design of next-generation wearable energy storage devices.

G. Y. Zhou, Dr. Y. E. Miao, L. L. Mo, F. L. Lai, Prof. T. X. Liu
State Key Laboratory for Modification of Chemical
Fibers and Polymer Materials
College of Materials Science and Engineering
Innovation Center for Textile Science and Technology
Donghua University
Shanghai 201620, P. R. China
E-mail: yuee_miao@dhu.edu.cn; txliu@dhu.edu.cn
Z. X. Wei, Prof. J. M. Ma
School of Physics and Electronics
Hunan University
Changsha 410082, P. R. China
E-mail: nanoelechem@hnu.edu.cn
Y. Wu
Research Center for Analysis and Measurement
Donghua University
Shanghai 201620, P. R. China

The ORCID identification number(s) for the author(s) of this article can be found under https://doi.org/10.1002/adfm.201804629.

1. Introduction

With the ever-increasing demand for flexible and wearable electronic devices, high-performance rechargeable lithium-ion batteries (LIBs) and sodium-ion batteries (SIBs) with unique advantages, such as portability, deformability, lightweight, and bendability, have drawn significant attentions in the past decade.[1] In tradition, the conventional cathodes are almost transition-metal oxide materials,[1a,d,2] however, they have the bottlenecks of limited capacity and resources, and serious environmental pollution. As an alternative, organic electrode materials have been considered as one kind of the most promising alternatives to traditional metal oxide materials due to their low cost and abundant resources, excellent structural versatility, better safety features and mechanical flexibility.[3] Furthermore, owing to the transformation of the Li$^+$/Na$^+$ storage mechanism from intercalation to chemical bond reactions, organic electrode materials are not restricted by the number of counterions and afterwards lead to significantly increased theoretical capacity.

Up to now, various types of organic materials such as conducting polymers,[4] organosulphur compounds,[3d,h] organic radical compounds,[5] and carbonyl compounds,[6] have been investigated as electrode materials for rechargeable LIBs/SIBs. Nevertheless, their electrochemical performance was hindered by the inherent poor electrical conductivity and easy dissolution of traditional organic electrodes with low molecular weight in organic electrolytes. Thus, the development of high-performance organic electrodes with good cyclic stabilities, stretchable and portable properties still remains a severe obstacle. Furthermore, SIBs display the sluggish kinetics due to the larger ionic radius of Na$^+$ compared to that of Li$^+$.[7] More dramatic and frequent structural changes are often accompanied in SIBs upon the electrochemical cycling. The slower diffusion and sodiation/desodiation of Na$^+$, in particular, may occur within the traditional bulk active particles and across the electrode. Therefore, it is highly desirable to develop ultrastable

ADVANCED
SCIENCE NEWS
www.advancedsciencenews.com

ADVANCED
FUNCTIONAL
MATERIALS
www.afm-journal.de

organic cathodes with designed nanoarchitectures and significantly enhanced charge/ion transport mechanisms for LIBs/SIBs, especially to accommodate the larger ionic radius of Na^+.

As an important class of organic electrode materials, conjugated carbonyl compounds have been considered as promising cathode materials for LIBs/SIBs with plenty of organic functional groups such as keto, carboxylate and anhydride. In particular, the superconjugated aromatic anhydride of 3,4,9,10-perylenetetracarboxylic dianhydride (PTCDA) which contains two conjugated anhydride groups and a perylene ring, was reported to be chemically stable during the lithiation and sodiation at the oxygen atoms of anhydride groups.[8–10] However, there has been a lack of detailed and integrated investigation on the molecular structure and electron localization function (ELF) changes of PTCDA during its electrochemical cycling processes for LIBs/SIBs. Herein, density functional theory (DFT) calculations have been carried out to track the whole discharge/charge processes of PTCDA cathode for LIBs/SIBs. As shown in **Figure 1**A, Li^+/Na^+ prefer to attack the diagonal carbonyl groups one by one in the anhydride groups of PTCDA, thus forming lithiated/sodiated PTCDA-Li/PTCDA-Na and PTCDA-Li$_2$/PTCDA-Na$_2$ products. Obviously, significantly enhanced density of states (DOS) are observed at the conduction band edges of PTCDA-Na (Figure S1A, Supporting Information) and PTCDA-Na$_2$ (Figure 1D) as compared to their counterparts of PTCDA-Li (Figure S1C, Supporting Information), PTCDA-Li$_2$ (Figure 1F) and pure PTCDA (Figure 1B). Correspondingly, the charge densities around the carbonyl groups in the anhydride groups of PTCDA-Na (Figure S1B, Supporting Information) and PTCDA-Na$_2$ (Figure 1C) are much higher than those of PTCDA-Li (Figure S1D, Supporting Information) and PTCDA-Li$_2$ (Figure 1E), indicating that electrons are more delocalized in the sodiated PTCDA molecules to achieve largely promoted electrical conductivity. Hence, PTCDA is chosen as an ideal active material to prepare the flexible organic cathodes in this work.

To further ameliorate the intrinsic low conductivity, sluggish electrochemical reaction kinetics and mechanical defects of organic electrode materials, an integrated bioinspired micro/nanofluidic system is designed based on the electrokinetic ion transport mechanisms inspired by a series of protein ion channels on cell membranes, and the hierarchical layered structure and strong interfacial interactions of nacre.[11] As displayed in **Figure 2**A, we report a highly flexible and binder-free composite film consisting of PTCDA/reduced graphene oxide (RGO)/carbon nanotubes (CNT) through vacuum filtration and heating processes, which is denoted as PTCDA/RGO/CNT. A three-dimensional (3D) interconnected micro/nanofluidic network is expected to be constructed all over the film as illustrated in Figure 2B. It is attributed to the noncovalent π–π stacking interaction between RGO nanosheets and CNTs. Indeed, the negatively charged RGO and CNTs will preferentially permeate counter Li^+/Na^+ ions, thus providing a highly conductive pathway for rapid diffusion and facilitated reaction of the electrolyte ions with PTCDA molecules in the composite film. When directly used as a flexible electrode, the PTCDA/RGO/CNT film presents good reversible capacities of 131 and 126 mA h g^{-1} at 10 mA g^{-1}, and superior rate capability of 49 and 32 mA h g^{-1} at 2000 mA g^{-1} for LIBs and SIBs, respectively. Furthermore, flexible lithium/sodium-ion full cells based on the PTCDA/RGO/CNT cathode and the lithiated/sodiated electrospun CNF anode have been demonstrated for the first time. To be emphasized, the lithium-ion full cell exhibits a wide working potential window of 1.90 V, a high specific capacity of 78.0 mA h g^{-1}, and a high Coulombic efficiency of 99% after 200 cycles at the large current density of 200 mA g^{-1}. Furthermore, the sodium-ion full cell shows a high specific capacity of 74.5 mA h g^{-1}, and a high Coulombic efficiency of 99% after 200 cycles at the large current density of 200 mA g^{-1}. The excellent electrochemical performance could be ascribed to the effective utilization of PTCDA and fast ion/electron transfer resulting from the unique porous micro/nanochannels of the sandwich-structured RGO and CNT frameworks.
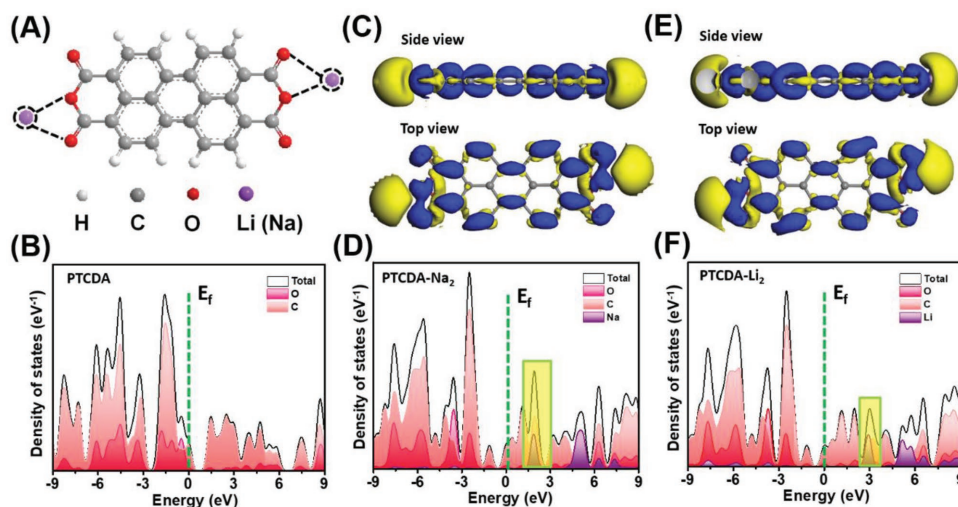

Figure 1. A) The proposed attack positions of Li^+/Na^+ in the molecular structure of PTCDA. Calculated DOS for B) PTCDA, D) PTCDA-Na$_2$, and F) PTCDA-Li$_2$. The shadowed region highlights the increased DOS at the conduction band edge of PTCDA-Na$_2$ and PTCDA-Li$_2$. The differential charge densities of C) PTCDA-Na$_2$, and E) PTCDA-Li$_2$.
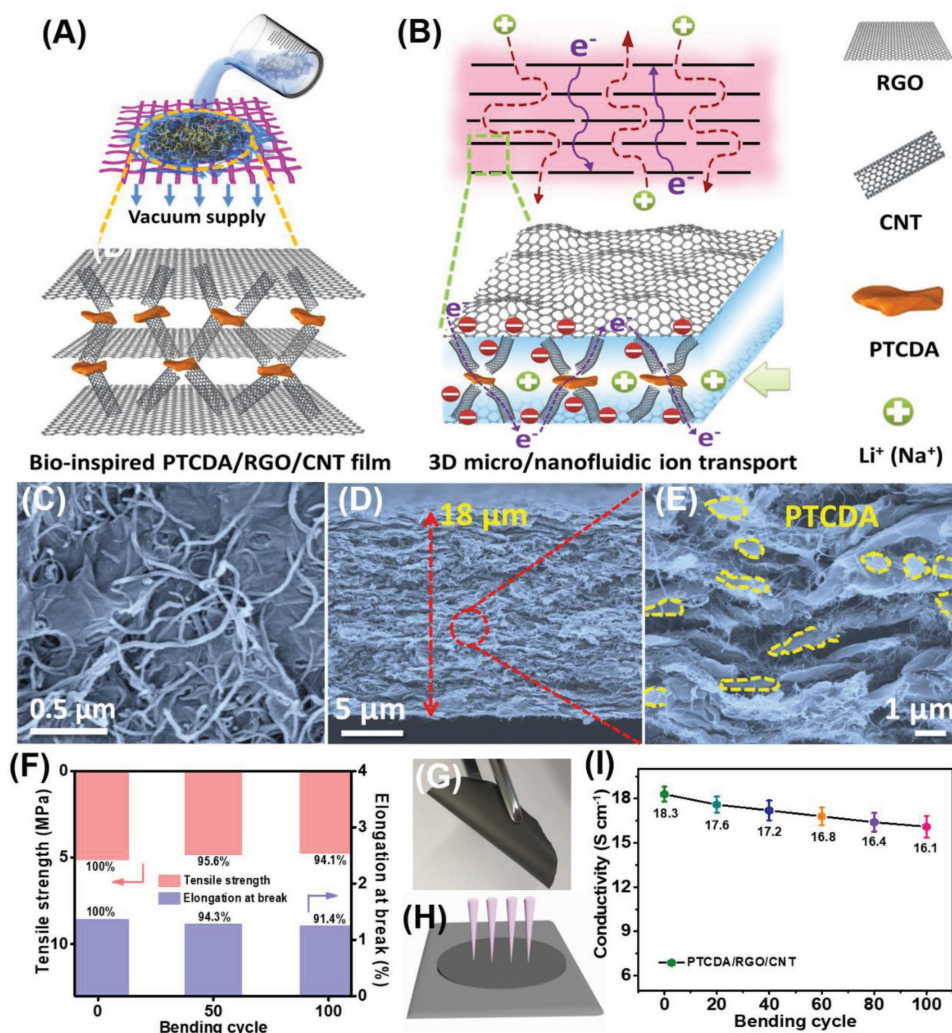
Figure 2. A,B) Schematic illustration for preparation of the bioinspired PTCDA/GO/CNT film with 3D micro/nanofluidic channels. SEM images of C) the in-plane, D) cross-sectional, and E) middle active layers of PTCDA/RGO/CNT composite film, respectively. F) The mechanical properties, and I) electrical conductivity of the flexible PTCDA/RGO/CNT film after different bending cycles. G) The digital photograph, and H) four-probe test model of the PTCDA/RGO/CNT film.

2. Results and Discussion

Inspired by the fast permeation of ions within the protein ion channels on cell membranes, we use a vacuum-assisted filtration method to fabricate the flexible sandwich-structured pristine PTCDA (PTCDA-pre)/GO/CNT film with bioinspired 3D multilayered micro/nanochannels. Then, heat treatment at 400 °C under Ar was carried out to obtain the PTCDA/RGO/CNT composites. As shown in Figure S2A,B of the Supporting Information, both of the Fourier transform infrared (FTIR) and ^{13}C nuclear magnetic resonance (NMR) spectra for PTCDA-pre and PTCDA show high uniformity in the peak position and intensity, indicating the outstanding thermal stability of PTCDA. Furthermore, the X-ray diffraction (XRD) pattern in Figure S2C of the Supporting Information demonstrates the same crystal structure of PTCDA before and after heat treatment with four diffraction peaks at $2\theta = 9.5°$, $12.4°$, $24.5°$, and $27.5°$, revealing the excellent structural stability

of PTCDA. Besides, the typical diffraction peak at $2\theta = 10.5°$ in the XRD pattern of GO/CNT is converted to a broad peak around $2\theta = 28°$ for RGO/CNT, implying the successful reduction of GO after heat-treated at 400 °C. Thermogravimetric analyzer (TGA) curves also indicate the excellent thermostability of PTCDA-pre which almost has no decomposition at 400 °C (Figure S2D, Supporting Information). Thus, based on the different weight losses of GO/CNT and PTCDA-pre/GO/CNT, the loading amount of PTCDA in the final PTCDA/RGO/CNT film is determined to be 50%.

Morphologies of the PTCDA/RGO/CNT film are shown in Figure 2C–E. To improve the conductivity and achieve the efficient utilization of PTCDA, CNTs are incorporated between RGO layers and PTCDA, which can both serve as the conductive linkers between the individual RGO sheets and PTCDA particles, and hinder the stack and aggregation of RGO sheets and PTCDA particles. As expected, the surface inspection of the PTCDA/RGO/CNT film (Figure 2C) reveals that CNTs

are tangled and interweaved with RGO sheets, forming a hierarchical network. Consequently, the RGO sheets and CNTs could function as the structural skeleton of the composite film, and at the same time serve as the long-range conducting network for electron transfer, as shown in Figure 2B. More importantly, a large number of micro/nanochannels are constructed by the interpenetrated RGO sheets and CNTs, which will effectively accelerate the penetration of electrolyte ions through the composite film. Figure 2D shows a typical cross-sectional scanning electron microscope (SEM) image of the PTCDA/RGO/CNT film, which exhibits an obvious sandwich-like architecture with an overall thickness of ≈18 μm. Moreover, PTCDA particles are stitched by RGO sheets and CNTs in the active layer (Figure 2E). Therefore, the unique architecture can substantially improve the conductivity and guarantee the effective utilization of active PTCDA particles, and maintain the mechanical and chemical structural stability during the following electrochemical cycling as well. As exhibited in Figure 2F, the as-prepared PTCDA/RGO/CNT film with 3D sandwich-structures exhibits good mechanical flexibility with 91.4% elongation at break, and even maintains the initial shape without any change after 100 bending cycles as displayed in Figure 2G. Furthermore, under a four-probe tester (Figure 2H), the PTCDA/RGO/CNT film also keeps a high in-plane conductivity of over 16.1 S cm^{-1} after 100 bending cycles (Figure 2I), indicating the potential as a freestanding and binder-free electrode for LIBs/SIBs. For comparison, PTCDA/RGO and PTCDA/CNT films have also been obtained by the same procedure. It is clear that the surface of PTCDA/RGO film displays a wave-like porous structure with multilayer RGO sheets corrugated together (Figure S3A, Supporting Information). Meanwhile, pore sizes ranging from sub-micrometers to several micrometers are observed from the interconnected 3D framework of RGO sheets and PTCDA in the cross-sectional images of PTCDA/RGO film (Figure S3B,C,

Supporting Information). However, ascribed to the large size of PTCDA (Figure S3D, Supporting Information) and week interlayer interactions, the PTCDA/CNT composite film exhibits poor mechanical properties and breaks into small pieces readily as shown in Figure S3E of the Supporting Information. Therefore, both of CNTs and RGO sheets play important roles in the acquisition of the flexible PTCDA/GO/CNT film with multilayer micro/nanofluidic ion transport channels and interconnected porous conductive frameworks. The much lower conductivity of PTCDA/RGO film compared to that of the PTCDA/RGO/CNT film further indicates CNTs can serve as the conductive linkers between the individual RGO sheet and PTCDA particles. To confirm the advantages of PTCDA over other organic materials in electronic conductivity, 1,4,5,8-naphthalenetetracarboxylic dianhydride (NTCDA) has been chosen as a control sample. Clearly, the conductivity of NTCDA/RGO/CNT film (Figure S3F, Supporting Information) is much lower than that of the PTCDA/RGO/CNT film tested by the four-probe tester, demonstrating the wise choice of PTCDA as a promising cathode material to prepare the flexible organic cathodes here.

The electrochemical performances of the composite films were evaluated using CR2032-type coin cells by cyclic voltammetry (CV) and galvanostatic discharge/charge measurements in the voltage range of 1.5–3.5 V versus Li/Li$^+$ or Na/Na$^+$. As shown in **Figure 3**A, the CV curves of PTCDA/RGO/CNT show a pair of reduction peaks at 2.38 and 2.29 V and a pair of oxidation peaks at 2.74 and 2.69 V from the second cycle, which corresponds to the continuous reduction/oxidation reaction steps of PTCDA with Li. Moreover, the CV curves overlap very well in the subsequent cycles, indicating an excellent reversible stability of the PTCDA/RGO/CNT electrode during the electrochemical reactions. Correspondingly, obvious voltage plateaus are observed around 2.38, 2.29 and 2.74, 2.69 V in the discharge
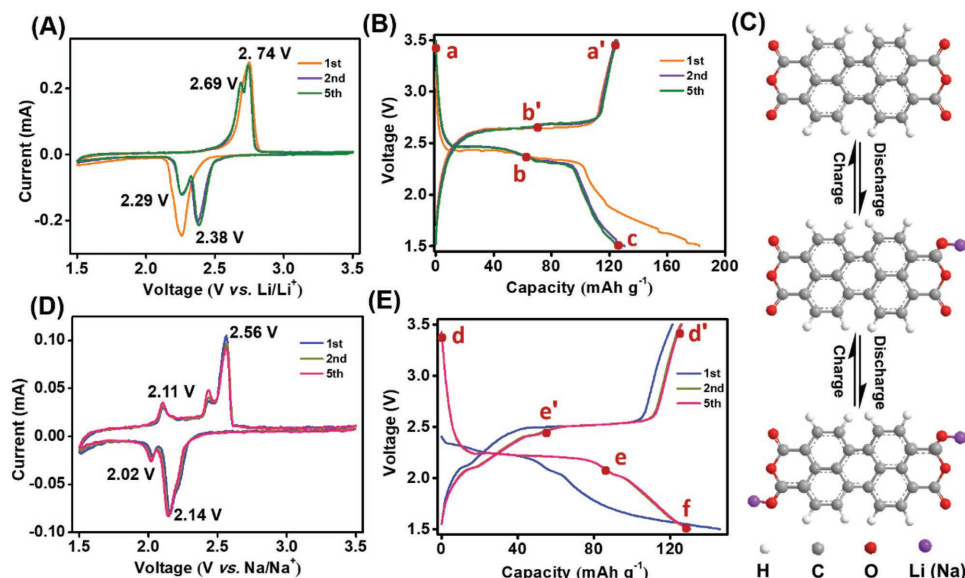

Figure 3. A,D) CV curves for the first, second, and fifth cycles of the PTCDA/RGO/CNT electrode for Li$^+$ and Na$^+$ storage at a scan rate of 0.1 mV s^{-1}, respectively. B,E) Galvanostatic discharge/charge curves of PTCDA/RGO/CNT for Li$^+$ and Na$^+$ storage at current density of 10 mA g^{-1}, respectively. The inset points indicate different discharge/charge states of the PTCDA/RGO/CNT electrode. C) The most possible redox mechanisms of PTCDA in LIBs and SIBs.

and the charge profiles of the PTCDA/RGO/CNT electrode (Figure 3B), further verifying the typical chemical bond reaction mechanisms between PTCDA and Li as illustrated in Figure 3C. Besides, the PTCDA/RGO/CNT electrode shows a high initial discharge capacity of 131 mA h g^{-1} at 10 mA g^{-1}, which is much higher than those of previously reported results as listed in Table S1 of the Supporting Information, indicating effective utilization of active PTCDA. For comparison, the CV and galvanostatic discharge/charge curves of RGO/CNT and PTCDA/RGO films are displayed in Figure S4 of the Supporting Information. It can be seen that the capacity of RGO/CNT can be almost neglected (Figure S4C, Supporting Information), while the PTCDA/RGO electrode exhibits only one pair of cathodic and anodic peaks (Figure S4B, Supporting Information) with a much lower initial discharge capacities of 103 mA h g^{-1} at 10 mA g^{-1} (Figure S4D, Supporting Information) compared to the PTCDA/RGO/CNT electrode. This well demonstrates that the incorporated CNTs between RGO layers and PTCDA can effectively improve the conductivity of PTCDA/RGO film and achieve the efficient utilization of PTCDA, which is quite consistent with the four-probe test result. Furthermore, ascribed to the facilitated ion permeation within the micro/nanochannel structures and superior conductivity of the RGO/CNT composite skeleton, the PTCDA/RGO/CNT electrode proves an outstanding electrochemical performance for SIBs as well. As shown in Figure 3D, two main reduction peaks occur at 2.14 and 2.02 V, while two oxidation peaks are observed at 2.11 and 2.56 V during the sodiation/desodiation processes. Meanwhile, the voltage profiles of PTCDA/RGO/

CNT in SIBs exhibit serial discharge voltage plateaus at 2.14 and 2.02 V, and charge voltage plateaus at 2.11 and 2.56 V, respectively (Figure 3E), which are quite consistent with the previously reported sequential one-electron reduction processes or two-electron reduction processes to form the radical anion (PTCDA$^-$) and radical dianion (PTCDA^{2-}) as displayed in Figure 3C.[6a,c,d] At the same time, the PTCDA/RGO/CNT electrode shows an outstanding discharge capacity of 126 mA h g^{-1} at 10 mA g^{-1}, being promising as an advanced electrode material for SIBs.

In order to well understand the redox reaction mechanisms in the LIBs and SIBs, ex situ FTIR spectra and X-ray photoelectron spectroscopy (XPS) measurements were carried out to reveal the discharge/charge processes of Li$^+$/Na$^+$ with PTCDA. As exhibited in the related ex situ FTIR spectra (**Figure 4**A) corresponding to different discharge/charge positions in Figure 3B for LIBs, a new signal appears near 515 cm^{-1} when the electrode is discharged from point a to c, which originates from the oscillation of Li—O bond formed by the carbonyl of PTCDA with Li$^+$ as listed in the molecular structure of Figure 3C.[12] Then, the peak disappears when the electrode is fully recharged from point c to a', revealing the reversible redox reactions from PTCDA-Li$_2$ to PTCDA during the charge process. Similarly, upon reacting with Li from point a to c, the survey XPS spectrum of the PTCDA/RGO/CNT electrode exhibits typical characteristics of C, O, and Li elements (Figure S5A, Supporting Information). Moreover, as for the C 1s spectra, the intensities of C=O (288.5 eV) and O—C=O (290.0 eV) peaks decrease and a new peak related to C=C—O—Li
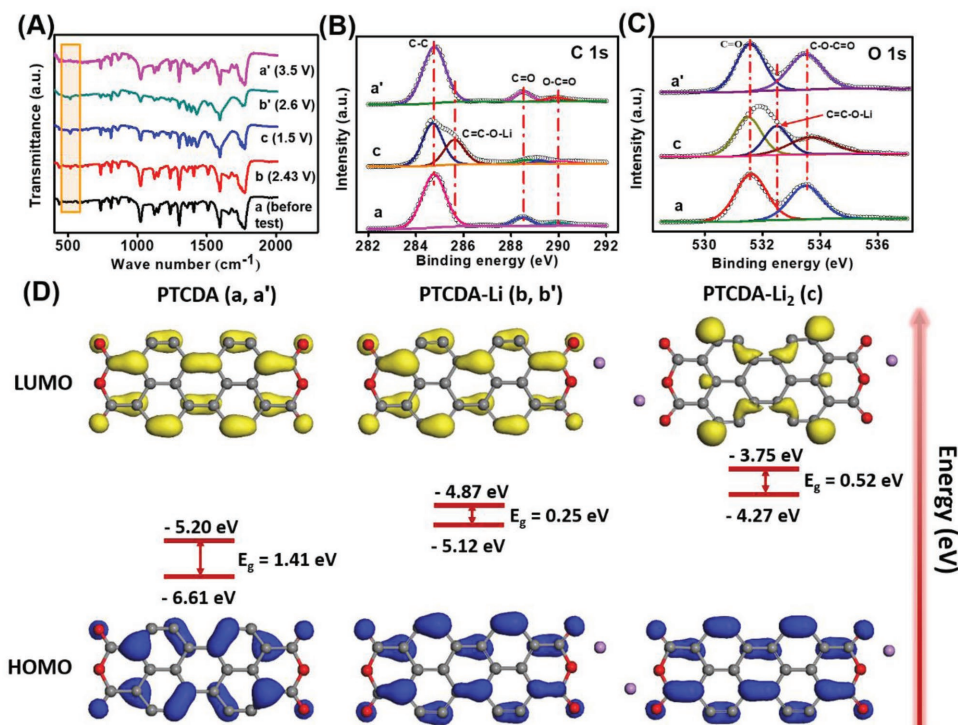

Figure 4. A) The ex situ FTIR, and B,C) XPS spectra of the PTCDA/RGO/CNT electrode for LIBs during the discharge/charge processes, respectively. D) Energy level diagrams of PTCDA for LIBs during the discharge/charge processes obtained by DFT calculations. E_g is the energy gap between HOMO and LUMO, which relates to the electron conductivity (smaller E_g means higher electron conductivity).

**ADVANCED
SCIENCE NEWS**

www.advancedsciencenews.com

**ADVANCED
FUNCTIONAL
MATERIALS**

www.afm-journal.de

appears at 285.6 eV from point *a* to *c* (Figure 4B). Subsequently, the intensities of C=O and O−C=O peaks increase and the C=C−O−Li peak disappears during the recharge process.[13] Meanwhile, a new peak is observed at 532.5 eV in the O1s spectrum of the PTCDA/RGO/CNT electrode during the discharge process (Figure 4C), which could be derived from the formation of C=C−O−Li.[13,14] After the removal of lithium during the recharge process, the C=C−O−Li peak disappears accompanied by the intensity increase of C=O (531.6 eV) and C−O−C=O (533.5 eV) peaks, further indicating the reversible lithiation of PTCDA.

In the same way, ex situ FTIR spectra and XPS measurements were carried out for the PTCDA/RGO/CNT electrode used for SIBs. As shown in Figure S6A of the Supporting Information, the peaks centered around 1700 and 1657 cm^{-1} corresponding to the carbonyl (C=O) asymmetric and stretching frequencies, respectively, are redshifted to a broad peak around 1637 cm^{-1} during discharge from point *d* to *f* as indicated in Figure 3E, implying the formation of a new bond between oxygen and sodium during the galvanostatic discharge process.[6a,c,d,7,15] After recharging back from point *f* to *d′*, the peaks around 1700 and 1657 cm^{-1} are recovered owing to the formation of C=O, which indicates the reversible redox reactions of PTCDA with Na during the discharge/charge processes. The survey XPS spectrum of PTCDA/RGO/CNT electrode exhibits the coexistence of C, O, and Na elements (Figure S5C, Supporting Information). Furthermore, as shown in Figure S6b of the Supporting Information, the decreased intensity of C=O and O−C=O peaks indicates the consumption of carbonyl groups when the electrode is discharged from the initial voltage (point *d*) to 1.5 V (point *f*). Meanwhile, a new broadening peak located at 285.55 eV, which is related to C=C−O−Na, emerges.[16] Then, the new peak related to C=C−O−Na disappears when the electrode is fully charged from point *f* to *d′*. In the O1s spectrum (Figure S6C, Supporting Information), the peak corresponding to the carbonyl group (C=O) becomes broadened and weak at the discharged state (point *f*), also implying the formation of a new bond (C=C−O−Na) between the oxygen and sodium species.[16,17] When recharged back to 3.5 V corresponding to point *d′*, all of these peaks recover to the original states, demonstrating an ideal reversible redox reaction of PTCDA with Na as well.

To better understand the variation in the plateau potentials of the organic cathode during discharge/charge processes, the band gap (*E*$_g$) values of the insertion and extraction of Li$^+$/Na$^+$ in PTCDA are obtained by DFT calculations. As provided in Figure 4D and Figure S6D (Supporting Information), the *E*$_g$ values between the highest occupied molecular orbital (HOMO) and the lowest unoccupied molecular orbital (LUMO) levels are 1.41, 0.52, and 0.47 eV for PTCDA, PTCDA-Li$_2$, and PTCDA-Na$_2$, respectively. As it has been reported that the electrode material possesses good conductivity when its *E*$_g$ value is lower than 2.5 eV,[18] PTCDA is demonstrated to be an ideal candidate for LIB and SIB applications here. Besides, an increased electronic conduction and a reduced polarization are observed for PTCDA-Na$_2$ compared to PTCDA-Li$_2$, which may lead to better redox reversibility and improved electrochemical property for PTCDA-Na$_2$ from the electronic conduction view.

However, from the ionic conduction view,[3f,g] SIBs have sluggish electrochemical reaction kinetics and poor cycling performance compared with LIBs due to the larger ionic radius of Na ion. Therefore, the PTCDA-based LIBs and SIBs are further evaluated under different current densities. Remarkably, as shown in **Figure 5**A, the PTCDA/RGO/CNT electrode delivers excellent rate capability and ultrahigh reversible capacities of 91 and 72 mA h g^{-1} at the current density of 200 mA g^{-1} for LIBs and SIBs, respectively. In addition, high specific capacities of 49 and 31 mA h g^{-1} can be retained for LIBs and SIBs, even at a high current density of 2000 mA g^{-1}. The excellent rate capability and superior capacity retention of PTCDA/RGO/CNT over PTCDA/RGO (Figure S7, Supporting Information) are ascribed to the unique 3D conducting micro/nanofluidic channels formed by RGO and CNTs as illustrated in Figure 5B. Exclusive and rapid migration paths are constructed for Li$^+$/Na$^+$ and largely improve conductivity and facilitate the lithiation/delithiation or sodiation/desodiation reactions of PTCDA in the designed bioinspired micro/nanofluidic channels. The superiority of the PTCDA/RGO/CNT electrode in kinetics is further analyzed by electrochemical impedance spectroscopy, in which much lower charge-transfer impedance of 150 Ω (Figure 5C) and much smaller Warburg coefficient of 20.4 (Figure S8A, Supporting Information) can be observed for the PTCDA/RGO/CNT electrode as compared to the large charge-transfer impedance of 188 Ω and Warburg coefficient of 31.8 for the PTCDA/RGO electrode in LIBs (Figure S8B,C, Supporting Information). That is to say that the introduction of CNTs in the PTCDA/RGO electrode can significantly facilitate the simultaneous transport of electrons and ions. Similarly, a low charge-transfer impedance of 400 Ω and a small Warburg coefficient of 39.2 have also been obtained for the PTCDA/RGO/CNT electrode in SIBs. Meanwhile, according to their corresponding CV curves obtained under different scan rates as shown in Figure S9 of the Supporting Information, high diffusion coefficients of Li$^+$ (1.83 × 10^{-12} cm^2 s^{-1}) and Na$^+$ (5.48 × 10^{-13} cm^2 s^{-1}) have been achieved for the PTCDA/RGO/CNT electrode in LIBs and SIBs, respectively (Figure 5D), further confirming the rapid ion transport through the 3D micro/nanofluidic channels.

Encouragingly, benefitting from the excellent mechanical strength and high conductivity of the PTCDA/RGO/CNT electrode as shown in Figure 2F,I, even after 500 cycles at a high current density of 200 mA g^{-1}, ultrastable reversible capacities of 65 and 90 mA h g^{-1} are retained with an average Coulombic efficiency approaching 100% for SIBs and LIBs (Figure 5E; Figure S10, Supporting Information), respectively. Especially, the field-emission scanning electron microscope (FESEM) and energy dispersive X-ray spectroscopy (EDS) mapping images verify the integrity of the electrodes after 500 cycling for SIBs and LIBs (Figure 5F,G; Figure S11, Supporting Information), in which no delamination of PTCDA, RGO, and CNT are observed. The satisfying strong structural integrity of the PTCDA/RGO/CNT electrode may be ascribed to the bioinspired 3D micro/nanofluidic channels with uniform porous structures, which can effectively accommodate severe volume changes of the active PTCDA during long-term redox reaction processes.

To explore the practical feasibility of the PTCDA/RGO/CNT electrode for flexible battery applications, full lithium/sodium-ion batteries were assembled using the PTCDA/RGO/CNT cathode coupled with electrochemically lithiated/sodiated CNFs as the anode (**Figure 6**A). The as-prepared
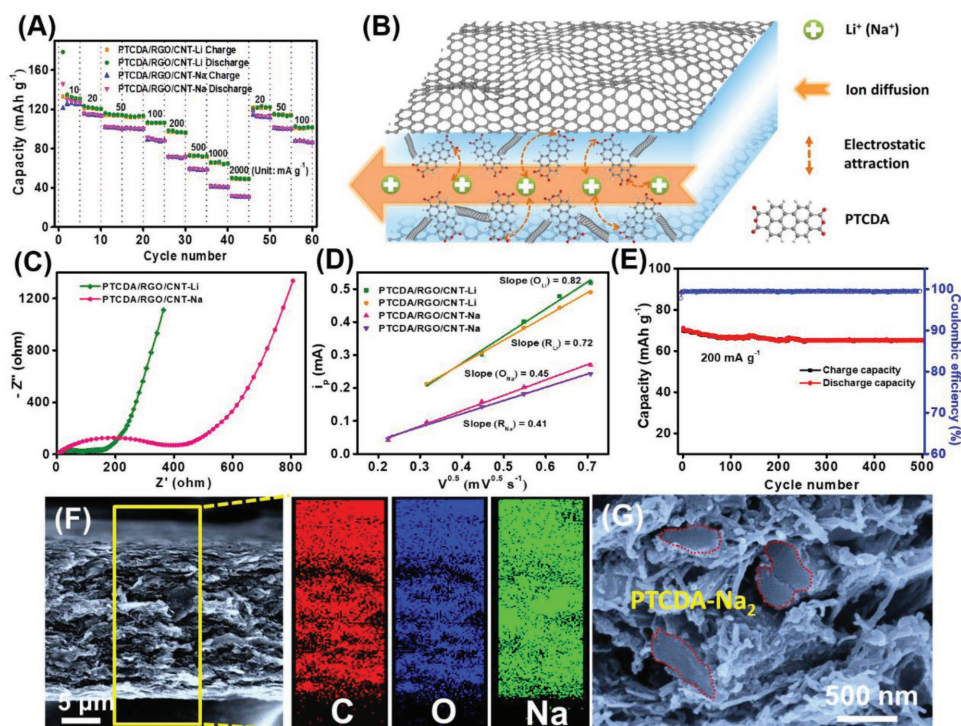
Figure 5. A) The rate performance of PTCDA/RGO/CNT electrode for LIBs and SIBs at different current densities. B) Schematic of the ion diffusion and electron transport in the 3D multilayer micro/nanofluidic channels. C) Nyquist plots of PTCDA/RGO/CNT for LIBs and SIBs, respectively. D) The linear relationship between the peak current (i_p) and the square root of the scan rate ($v^{1/2}$) of PTCDA/RGO/CNT for LIBs and SIBs, respectively. E) The cycling stability of PTCDA/RGO/CNT for SIBs at a current density of 200 mA g^{-1}. F,G) The cross-sectional SEM images and corresponding ex situ EDS mappings of carbon, oxygen, and sodium of the PTCDA/RGO/CNT electrode after 500 cycles in SIBs.

CNF membrane exhibits excellent mechanical property (Figure S12A, Supporting Information) and high conductivity (Figure S12B, Supporting Information), thus contributing to the stable specific discharge capacities for the half cell configurations of LIBs and SIBs (Figure S13, Supporting Information).

Based on the optimized weight ratio of 1.7:1 between the cathode and the anode materials, the electrochemical performance of the PTCDA/RGO/CNT//CNFs-Li full cell was evaluated between 1.0 and 3.0 V. As shown in Figure 6B, the CV curves show a pair of anodic peaks assigned at 1.89 and 1.94 V
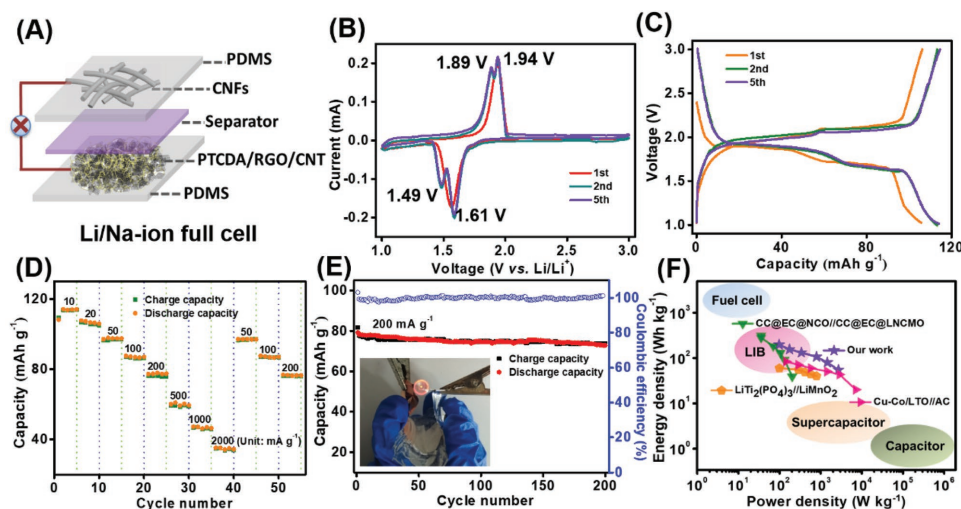

Figure 6. A) Schematic architecture of the flexible lithium/sodium-ion full cells assembled with the PTCDA/RGO/CNT cathode and CNF anode. Electrochemical performances of the PTCDA/RGO/CNT//CNFs-Li full cell. B) CV curves for the first, second, and fifth cycles of the full cell at a scan rate of 0.1 mV s^{-1}. C) Galvanostatic discharge/charge curves of the full cell at current density of 10 mA g^{-1}. D) The rate performance of the full cell at different current densities. E) The cycling stability of the full cell at a current density of 200 mA g^{-1}. F) Ragone plots of our work compared to other previously reported full-cell LIB devices.

and cathodic peaks at 1.49 and 1.61 V, respectively. The narrow potential gaps between the peaks demonstrate the low polarization between the electrode and the electrolyte, which illustrates the small charge-transfer impedance (Figure S14A, Supporting Information) and high ion diffusion rate (Figure S14B, Supporting Information) of the PTCDA/RGO/CNT//CNFs-Li full cell. In particular, the full cell exhibits an initial discharge capacity of 114.5 mA h g^{-1} at the current density of 10 mA g^{-1} and excellent rate performance of 35 mA h g^{-1} at the current density of 2000 mA g^{-1} based on the weight of the active materials (Figure 6C,D). More importantly, a high specific capacity of 78.0 mA h g^{-1} with a Coulombic efficiency of 99% are obtained after 200 cycles at a high current density of 200 mA g^{-1} (Figure 6E), and could turn on a 2.0 V light emitting diode (LED) (inset in Figure 6E). Notably, the full cell exhibits a high specific energy density of 132.6 W h kg^{-1} at the power density of 340 W kg^{-1} (Figure 6F), being much higher than many of the recently reported LIB full cell devices.[19] Similarly, based on the optimized weight ratio of 1.8:1 between the cathode and anode materials, the electrochemical performance of the PTCDA/RGO/CNT//CNFs-Na full cell was evaluated between 0.7 and 2.7 V. The PTCDA/RGO/CNT//CNFs-Na full cell also exhibits excellent reversibility (Figure S15A,B, Supporting Information), excellent rate performance, and cycling stability with a Coulombic efficiency of 99% after 200 cycles at a high current density of 200 mA g^{-1} (Figure S15C,D, Supporting Information). This can also be attributed to the low charge-transfer impedance (Figure S14A, Supporting Information) and fast ion diffusion rate (Figure S14B, Supporting Information) of the PTCDA/RGO/CNT//CNFs-Na full cell.

3. Conclusions

In summary, we report a newly designed organic cathode with bioinspired sandwich-like architectures for rechargeable LIB and SIB applications. With the micro/nanofluidic ion transport channels developed through a facile vacuum-assisted filtration method, the PTCDA/RGO/CNT electrode displays fast Li$^+$/Na$^+$ diffusion kinetics, and the resulting high reversible specific capacities, excellent rate performances and outstanding cycling stabilities. Furthermore, assembled by the mechanically robust PTCDA/RGO/CNT cathode and CNFs anode, the flexible PTCDA/RGO/CNT//CNFs-Li full cell delivers a high specific energy density of 132.6 W h kg^{-1} at the power density of 340 W kg^{-1}, being much superior compared to many previous LIB full cell devices. Moreover, the PTCDA/RGO/CNT//CNFs-Na full cell also delivers a high specific energy density of 104.4 W h kg^{-1} at the power density of 288 W kg^{-1}. Therefore, this work demonstrates the development of a bioinspired organic cathode with micro/nanofluidic ion transport channels for energy-efficient rechargeable batteries from both experimental and theoretical views, which provides basal guidelines for the future design of high-performance organic electrodes.

4. Experimental Section

Materials: Multiwalled carbon nanotubes were supplied by Chengdu Institute of Organic Chemistry, Chinese Academy of Sciences, China. Natural graphite powder (325 mesh) was purchased from Alfa-Aesar. The raw materials of 3,4,9,10-perylenetetracarboxylic and 1,4,5,8-naphthalenetetracarboxylic dianhydride, which are denoted as PTCDA-pre and NTCDA-pre, respectively, was obtained from TCI, Tokyo Chemical Industry Co., Ltd, Tokyo, Japan. The elastomer prepolymer of polydimethylsiloxane (PDMS, Sylgard 184) was purchased from Dow Corning and used without any further purification. Deionized water was used throughout all the experiments. All the reagents were of analytical grade and used without further purification.

Synthesis of PTCDA/RGO/CNT and PTCDA/RGO Films: GO was prepared from natural graphite powder using the modified Hummers, method according to previous report.[20] CNT of 10–20 nm in diameter and 10–30 μm in length was surface-modified by the mixture of H$_2$SO$_4$/HNO$_3$ (3/1, v/v).[21] PTCDA-pre was directly used without future purification. In a typical preparation process, 320 mg of the as-prepared GO and 80 mg of CNT were dispersed in 200 mL of *N*-methyl pyrrolidone by sonication in a 40 kHz ultrasonic bath for 10 h. Then, 150 mg of PTCDA-pre was added into 150 mL of the above GO/CNT dispersion under Ar atmosphere and magnetically stirred for 2 h at room temperature to obtain PTCDA-pre/GO/CNT dispersion.

To obtain the PTCDA/RGO/CNT film, GO/CNT, PTCDA-pre/GO/CNT, and GO/CNT dispersions were sequentially vacuum-filtrated through a polyester filter membrane with 2.5 μm pore size. Typically, 16 mg of the as-prepared GO and 4 mg of CNT were dispersed in 40 mL of *N*-methyl pyrrolidone by sonication in a 40 kHz ultrasonic bath for 10 h to obtain the GO/CNT dispersion. Then, 2 mL of GO/CNT dispersion was vacuum-filtrated through a polyester filter membrane. After draining the GO/CNT dispersion, 10 mL of PTCDA-pre/GO/CNT dispersion and 2 mL of GO/CNT dispersion were sequentially vacuum-filtrated by the same procedure with the first step. The as-obtained film was dried at 80 °C in a vacuum oven, and heat-treated at 400 °C under Ar for 2 h to obtain the PTCDA/RGO/CNT composite with a 50 wt% loading amount of PTCDA. To show the positive effects of CNT and RGO sheets, PTCDA/RGO and PTCDA/CNT films were also prepared using the same procedure. Furthermore, another organic material of NTCDA has been chosen as a control sample to prepare the NTCDA/RGO/CNT film.

Synthesis of Lithiated/Sodiated Electrospun CNFs: The freestanding electrospun CNFs membrane was prepared as previously reported.[22] Briefly, polyacrylonitrile nanofiber membrane was prepared by electrospinning at a concentration of 10 wt%. Then, it was preoxidized under air atmosphere at a heating rating of 1 °C min^{-1} to 230 °C and maintained for 3 h, and carbonized under vacuum with a heating rate of 15 °C min^{-1} to 1000 °C and maintained for 1 h, thus resulting in the flexible CNF membrane with excellent electrical and mechanical properties. The lithiation/sodiation of CNFs was carried out by discharging the CNF electrode to the full capacity (0.01 V vs Li$^+$/Li) or (0.01 V vs Na$^+$/Na) in a half-cell configuration. Then, the lithiated/sodiated CNFs was recycled from the cycled half-cell inside an Ar-filled glove box, and directly used as the anode for assembly of the full-cell at room temperature.

Characterizations: Morphology features of the PTCDA/RGO/CNT and PTCDA/RGO films were observed using a FESEM (HitachiS-8010) equipped with an EDS detector. FTIR spectra of the samples were performed using a Nicolet 8700 FTIR spectrometer. ^{13}C NMR spectra were collected using a BrukerAvance 400 nuclear magnetic resonance spectrometer. The crystalline structure and constitutes of the samples were measured by using powder XRD (Bruker D8 Advance) and NETZSCH TG 209 F1 Libra TGA with a temperature ramp of 10 °C min^{-1} under N$_2$ atmosphere, respectively. Mechanical properties of the PTCDA/RGO/CNT film and CNF membrane were measured by a universal testing machine (SANS, Shenzhen, China) at a tensile speed of 5 mm min^{-1}. Electrical conductivities of the PTCDA/RGO/CNT film and CNF membrane were measured by a four-point probes resistivity measurement system (RST-8 model, Guangzhou four-point probe technology Co., LTD, China).

Theoretical Calculation Details: DFT calculations were carried out with Vienna ab initio simulation package.[23] The exchange-correlation function was described by the Perdew–Burke–Ernzerhof based on generalized

gradient approximation method. The interaction between the core electrons and the valence electrons was described using the frozen-core projector-augmented wave method.[24] Wave functions were expanded in a plane wave basis and the cut-off energy was set to 400 eV. The convergence criterion was set at 10^{-5} eV for the total energy calculations. The vacuum region was set to 15 Å to remove the interactions between periodic slabs. The adsorption energy (E_{ad}) of the Li and Na atoms at the sites in PTCDA was calculated as follows: $E_{ad} = E_{PTCDA-Li(Na)} - (E_{PTCDA} + E_{Li(Na)})$, where E_{PTCDA}, $E_{Li(Na)}$, and $E_{PTCDA-Li(Na)}$ are the total energies for pure PTCDA, one Li(Na) atom, and different adsorption sites with one or two Li(Na) atom in PTCDA, respectively.

Electrochemical Tests: The PTCDA/RGO/CNT film was cut into round slices with a diameter of 12 mm and directly used as electrodes for the assembly of CR2032 coin-type batteries. For LIBs, metallic lithium was used as the counter electrode, polypropylene film (Celgard 2400) as the separator, and 1 M LiPF$_6$ in ethylene carbonate (EC)/dimethyl carbonate (DMC) (1:1, v/v) as the electrolyte. For SIBs, metallic sodium foil was used as the counter electrode, 1 M NaClO$_4$ in EC:DMC (1:1, v/v) with 5.0% FEC as the electrolyte, and a glass fiber (Whatman) as the separator. The cells were assembled in an argon-filled glove box with moisture and oxygen content below 0.1 ppm. The flexible full cell was assembled by using the flexible lithiated/sodiated CNFs as the anode and PTCDA/RGO/CNT film as the cathode. Here, PDMS elastomer wa s used as the sealing agent, which was synthesized by preparing a mixture of PDMS precursor and thermal curing agent with a mass ratio of 10:1, and then heat-treated at 130 °C for 30 min in a convection oven. Galvanostatic discharge–charge experiments were conducted in the potential range from 1.5 to 3.5 V at different current rates using a Land CT-2001A (Wuhan, China) Instruments testing system. CV was conducted using an Arbin Instruments testing system (Arbin-SCTS). Electrochemical impedance spectroscopy (0.01 Hz–100 kHz, 5 mV) measurements were performed on an electrochemical workstation (CHI 760D). In addition, all the cells were held at open circuits and room temperature for 12 h before electrochemical tests. The specific capacities were calculated based on the weight of active materials. The energy density of the full cell was calculated based on the following equation

$$E = C \times U \tag{1}$$

where E is the energy density of the full cell (W h kg^{-1}), C is the discharge specific capacity of the full cell (mA h g^{-1}), and U is the corresponding operational voltage window of the full cell (V).

Supporting Information

Supporting Information is available from the Wiley Online Library or from the author.

Acknowledgements

Conflict of Interest

The authors declare no conflict of interest.

[1] a) M. Koo, K. I. Park, S. H. Lee, M. Suh, D. Y. Jeon, J. W. Choi, K. Kang, K. J. Lee, *Nano Lett.* **2012**, *12*, 4810; b) X. Wang, X. Lu, B. Liu, D. Chen, Y. Tong, G. Shen, *Adv. Mater.* **2014**, *26*, 4763; c) L. Wang, Y. Zhang, J. Pan, H. Peng, *J. Mater. Chem. A* **2016**, *4*, 13419; d) H. Li, Y. Ding, H. Ha, Y. Shi, L. Peng, X. Zhang, C. J. Ellison, G. Yu, *Adv. Mater.* **2017**, *29*, 1700898; e) H. Gao, T. Zhou, Y. Zheng, Y. Liu, J. Chen, H. Liu, Z. Guo, *Adv. Energy Mater.* **2016**, *6*, 1601037; f) Y. Yang, X. Liu, Z. Zhu, Y. Zhong, Y. Bando, D. Golberg, J. Yao, X. Wang, *Joule* **2018**, *2*, 1075.

[2] a) W. Zhang, J. Mao, S. Li, Z. Chen, Z. Guo, *J. Am. Chem. Soc.* **2017**, *139*, 3316; b) P. Lu, Y. Sun, H. Xiang, X. Liang, Y. Yu, *Adv. Energy Mater.* **2018**, *8*, 1702434; c) Y. Z. Sheng, Y. Yin, J. Kong, C. Zou, C. Li, X. Lu, J. Ma, F. Y. C. Boey, X. Chen, *ACS Nano* **2011**, *5*, 4350; d) Y. Tang, Y. Zhang, J. Deng, J. Wei, H. L. Tam, B. K. Chandran, Z. Dong, Z. Chen, X. Chen, *Adv. Mater.* **2014**, *26*, 6111; e) M. Zheng, H. Tang, Q. Hu, S. Zheng, L. Li, J. Xu, H. Pang, *Adv. Funct. Mater.* **2018**, *28*, 1707500; f) S. Zheng, X. Li, B. Yan, Q. Hu, Y. Xu, X. Xiao, H. Xue, H. Pang, *Adv. Energy Mater.* **2017**, *7*, 1602733; g) W. Li, S. Hu, X. Luo, Z. Li, X. Sun, M. Li, F. Liu, Y. Yu, *Adv. Mater.* **2017**, *29*, 1605820; h) L. Wang, Y. G. Sun, L. L. Hu, J. Y. Piao, J. Guo, A. Manthiram, J. M. Ma, A. M. Cao, *J. Mater. Chem. A* **2017**, *5*, 8752.

[3] a) Y. Liang, Z. Tao, J. Chen, *Adv. Energy Mater.* **2012**, *2*, 742; b) W. Huang, Z. Zhu, L. Wang, S. Wang, H. Li, Z. Tao, J. Shi, L. Guan, J. Chen, *Angew. Chem., Int. Ed.* **2013**, *52*, 9162; c) J. K. Kim, Y. Kim, S. Park, H. Ko, Y. Kim, *Energy Environ. Sci.* **2016**, *9*, 1264; d) T. Ma, Q. Zhao, J. Wang, Z. Pan, J. Chen, *Angew. Chem., Int. Ed.* **2016**, *55*, 6428; e) E. C. Montoto, G. Nagarjuna, J. Hui, M. Burgess, N. M. Sekerak, K. Hernandez-Burgos, T. S. Wei, M. Kneer, J. Grolman, K. J. Cheng, J. A. Lewis, J. S. Moore, J. Rodriguez-Lopez, *J. Am. Chem. Soc.* **2016**, *138*, 13230; f) T. B. Schon, B. T. McAllister, P. F. Li, D. S. Seferos, *Chem. Soc. Rev.* **2016**, *45*, 6345; g) Y. Wang, Y. Ding, L. Pan, Y. Shi, Z. Yue, Y. Shi, G. Yu, *Nano Lett.* **2016**, *16*, 3329; h) M. Wu, Y. Cui, A. Bhargav, Y. Losovyj, A. Siegel, M. Agarwal, Y. Ma, Y. Fu, *Angew. Chem., Int. Ed.* **2016**, *55*, 10027; i) C. Peng, G. H. Ning, J. Su, G. Zhong, W. Tang, B. Tian, C. Su, D. Yu, L. Zu, J. Yang, M. F. Ng, Y. S. Hu, Y. Yang, M. Armand, K. P. Loh, *Nat. Energy* **2017**, *2*, 17074; j) Y. Cui, J. D. Ackerson, Y. Ma, A. Bhargav, J. A. Karty, W. Guo, L. Zhu, Y. Fu, *Adv. Funct. Mater.* **2018**, *28*, 1801791.

[4] a) Q. Zhao, Y. Lu, J. Chen, *Adv. Energy Mater.* **2017**, *7*, 1601792; b) Z. Wang, C. Xu, P. Tammela, P. Zhang, K. Edström, T. Gustafsson, M. Strømme, L. Nyholm, *Energy Technol.* **2015**, *3*, 563.

[5] a) S. Bahceci, B. Esat, *J. Power Sources* **2013**, *242*, 33; b) L. Xu, F. Yang, C. Su, L. Ji, C. Zhang, *Electrochim. Acta* **2014**, *130*, 148.

[6] a) B. Tian, G. H. Ning, W. Tang, C. Peng, D. Yu, Z. Chen, Y. Xiao, C. Su, K. P. Loh, *Mater. Horiz.* **2016**, *3*, 429; b) Q. Zhao, Z. Zhu, J. Chen, *Adv. Mater.* **2017**, *29*, 1607007; c) H. Banda, D. Damien, K. Nagarajan, M. Hariharan, M. M. Shaijumon, *J. Mater. Chem. A* **2015**, *3*, 10453; d) H. Wang, P. Hu, J. Yang, G. Gong, L. Guo, X. Chen, *Adv. Mater.* **2015**, *27*, 2348.

[7] a) K. T. Lee, T. N. Ramesh, F. Nan, G. Botton, L. F. Nazar, *Chem. Mater.* **2011**, *23*, 3593; b) Y. Park, D. S. Shin, S. H. Woo, N. S. Choi, K. H. Shin, S. M. Oh, K. T. Lee, S. Y. Hong, *Adv. Mater.* **2012**, *24*,

3562; c) H. G. Wang, S. Yuan, Z. Si, X. B. Zhang, *Energy Environ. Sci.* **2015**, *8*, 3160.

[8] X. Han, C. Chang, L. Yuan, T. Sun, J. Sun, *Adv. Mater.* **2007**, *19*, 1616.

[9] W. Luo, M. Allen, V. Raju, X. Ji, *Adv. Energy Mater.* **2014**, *4*, 1400554.

[10] Y. Chen, W. Luo, M. Carter, L. Zhou, J. Dai, K. Fu, S. Lacey, T. Li, J. Wan, X. Han, Y. Bao, L. Hu, *Nano Energy* **2015**, *18*, 205.

[11] a) W. Guo, C. Cheng, Y. Wu, Y. Jiang, J. Gao, D. Li, L. Jiang, *Adv. Mater.* **2013**, *25*, 6064; b) S. Gong, Q. Cheng, *Compos. Commun.* **2018**, *7*, 16; c) J. Liu, N. Wang, L. J. Yu, A. Karton, W. Li, W. Zhang, F. Guo, L. Hou, Q. Cheng, L. Jiang, D. A. Weitz, Y. Zhao, *Nat. Commun.* **2017**, *8*, 2011; d) S. Wan, J. Peng, L. Jiang, Q. Cheng, *Adv. Mater.* **2016**, *28*, 7862; e) Q. Cheng, M. Wu, M. Li, L. Jiang, Z. Tang, *Angew. Chem., Int. Ed.* **2013**, *52*, 3750.

[12] a) M. Armand, S. Grugeon, H. Vezin, S. Laruelle, P. Ribiere, P. Poizot, J. M. Tarascon, *Nat. Mater.* **2009**, *8*, 120; b) S. Wang, L. Wang, K. Zhang, Z. Zhu, Z. Tao, J. Chen, *Nano Lett.* **2013**, *13*, 4404.

[13] a) C. Zhan, J. Lu, A. Jeremy Kropf, T. Wu, A. N. Jansen, Y. K. Sun, X. Qiu, K. Amine, *Nat. Commun.* **2013**, *4*, 2437; b) Q. C. Liu, J. J. Xu, S. Yuan, Z. W. Chang, D. Xu, Y. B. Yin, L. Li, H. X. Zhong, Y. S. Jiang, J. M. Yan, X. B. Zhang, *Adv. Mater.* **2015**, *27*, 5241.

[14] S. H. Ha, Y. S. Jeong, Y. J. Lee, *ACS Appl. Mater. Interfaces* **2013**, *5*, 12295.

[15] H. G. Wang, S. Yuan, D. L. Ma, X. L. Huang, F. L. Meng, X. B. Zhang, *Adv. Energy Mater.* **2014**, *4*, 1301651.

[16] S. Wu, W. Wang, M. Li, L. Cao, F. Lyu, M. Yang, Z. Wang, Y. Shi, B. Nan, S. Yu, Z. Sun, Y. Liu, Z. Lu, *Nat. Commun.* **2016**, *7*, 13318.

[17] T. Sun, Z. J. Li, H. G. Wang, D. Bao, F. L. Meng, X. B. Zhang, *Angew. Chem., Int. Ed.* **2016**, *55*, 10662.

[18] W. Zhang, P. Sun, S. Sun, *Comput. Mater. Sci.* **2017**, *134*, 42.

[19] a) J. Y. Luo, Y. Y. Xia, *Adv. Funct. Mater.* **2007**, *17*, 3877; b) M. S. Balogun, H. Yang, Y. Luo, W. Qiu, Y. Huang, Z. Q. Liu, Y. Tong, *Energy Environ. Sci.* **2018**, *11*, 1859; c) C. A. Zhou, X. Xia, Y. Wang, Z. Yao, J. Wu, X. Wang, J. Tu, *Small* **2018**, *14*, 1704339.

[20] D. A. Dikin, S. Stankovich, E. J. Zimney, R. D. Piner, G. H. Dommett, G. Evmenenko, S. T. Nguyen, R. S. Ruoff, *Nature* **2007**, *448*, 457.

[21] J. Liu, A. G. Rinzler, H. Dai, J. H. Hafner, R. K. Bradley, P. J. Boul, A. Lu, T. Iverson, K. Shelimov, C. B. Huffman, *Science* **1998**, *280*, 1253.

[22] Z. Zhou, C. Lai, L. Zhang, Y. Qian, H. Hou, D. H. Reneker, H. Fong, *Polymer* **2009**, *50*, 2999.

[23] a) G. Kresse, J. Hafner, *Phys. Rev. B* **1993**, *47*, 558; b) G. Kresse, J. Furthmüller, *Comput. Mater. Sci.* **1996**, *6*, 15; c) C. Y. Cui, Z. X. Wei, J. T. Xu, Y. Q. Zhang, S. H. Liu, H. K. Liu, M. L. Mao, S. Y. Wang, J. M. Ma, S. X. Dou, *Energy Storage Mater.* **2018**, *15*, 22; d) Z. Su, Z. X. Wei, C. Lai, H. Q. Deng, Z. X. Liu, J. M. Ma, *Energy Storage Mater.* **2018**, *14*, 129.

[24] a) G. Kresse, D. Joubert, *Phys. Rev. B* **1999**, *59*, 1758; b) P. E. Blöchl, *Phys. Rev. B* **1994**, *50*, 17953.